



# Nanopore characterization of mine roof shales by SANS, nitrogen adsorption, and mercury intrusion: Impact on water adsorption/retention behavior



Guijie Sang<sup>a</sup>, Shimin Liu<sup>a,\*</sup>, Rui Zhang<sup>a</sup>, Derek Elsworth<sup>a</sup>, Lilin He<sup>b</sup>

<sup>a</sup> Department of Energy and Mineral Engineering, G<sup>3</sup> Center and Energy Institute, The Pennsylvania State University, University Park, PA 16802, USA

<sup>b</sup> Neutron Scattering Division, Oak Ridge National Laboratory, Oak Ridge, TN 37830, USA

## ARTICLE INFO

### Keywords:

Small angle neutron scattering  
Strength reduction  
Water retention  
Pore structure  
Pore size distribution  
Specific surface area

## ABSTRACT

Moisture-induced reduction in the strength of shales is one of the primary mechanisms of roof degradation affecting the stability and safety of underground coal mines. The underlying mechanisms of nanoscale matrix-water interactions remains unclear. Thus, an improved understanding of the nanopore structure, and dependent water adsorption and retention behavior of shale is key in defining strength degradation due to seasonal variations in humidity and temperature in underground coal mines. We use small-angle neutron scattering (SANS), low-pressure N<sub>2</sub> adsorption (LPNA), and high-pressure mercury intrusion porosimetry (MIP) to characterize the nanopore structure of a fireclay (7F) and four coal mine roof shales (6R, 5A, 6F, H6) from the Illinois basin. The results show that overall distributions of pore volume obtained from SANS, LPNA and MIP techniques agree well between methods and over a wide range of pore size from ~1 nm to ~100 nm. Mercury porosities for the five ordered (7F, 6R, 5A, 6F, H6) samples (7.3%, 7.8%, 8.3%, 12.3%, 4.6%) are higher than the respective N<sub>2</sub> porosities (5.0%, 6.3%, 3.8%, 8.2%, 2.5%), as attributed to the dilation of mesopores and compression of the grain skeleton induced by high pressure intrusion of mercury. The SANS porosities for samples 7F, 6R, 5A, 6F (4.0%, 6.2%, 4.1%, 8.8%) are in good agreement with their N<sub>2</sub> porosities. Among all tested samples, H6 shale exhibits a relatively high SANS porosity (8.0%) but the lowest N<sub>2</sub> (2.5%) and mercury porosities (4.6%). This is attributed to the interlayer micro-pore spaces within montmorillonite, which is detected by SANS but not by the two fluid penetration methods due to the inaccessibility of N<sub>2</sub> molecules and mercury. Based on LPNA, larger micropores (1.5–2 nm) and mesopores (2–50 nm) predominantly contribute to the total porosity (~77.8%–87.6%) for the five tested samples.

The water adsorption isotherms are measured by dynamic vapor sorption (DVS) and water retention curves are calculated based on the characterized pore size distribution (PSD) by LPNA and MIP techniques. Pore structures of the five studied samples evidently exert a strong influence on their water adsorption and retention behaviors. Water adsorption capacity correlates positively with total porosity/specific surface area (SSA), with a large proportion of micro/meso-pores resulting in the strong water retention capacity with matric suction reaching ~100–150 MPa for liquid saturation < 3%. Among the studied fireclay/shales, samples with higher retention capacity tend to adsorb more water. Thus, nanopore structure and its impact on water adsorption and retention behavior exert the key controls on shale-water interaction and its implication on strength reduction of roof shales in underground coal mines.

## 1. Introduction

The Mine Safety and Health Administration (MSHA) reports that nearly 11,600 non-injury roof falls occurred in nearly 800 active coal mines from 1999 to 2008 (Bajpayee et al., 2014). Although falling roofs cause no direct fatality or injury to coal miners, massive non-injury roof

falls over extended periods disrupt regular mining activity, impair ventilation, impede passage of miners, and cause other potential ground control problems (Molinda, 2003). Most roof fall incidents occur due to several factors such, including slip in the roof, laminated roof, draw rock, wet roof, rider seam, clay veins and horizontal-stress-induced cutter failures (Molinda, 2003; Iannacchione et al., 2005; Esterhuizen

\* Corresponding author.

E-mail address: [szl3@psu.edu](mailto:szl3@psu.edu) (S. Liu).

<https://doi.org/10.1016/j.coal.2018.11.009>

Received 14 July 2018; Received in revised form 11 November 2018; Accepted 11 November 2018

Available online 12 November 2018

0166-5162/ © 2018 Elsevier B.V. All rights reserved.

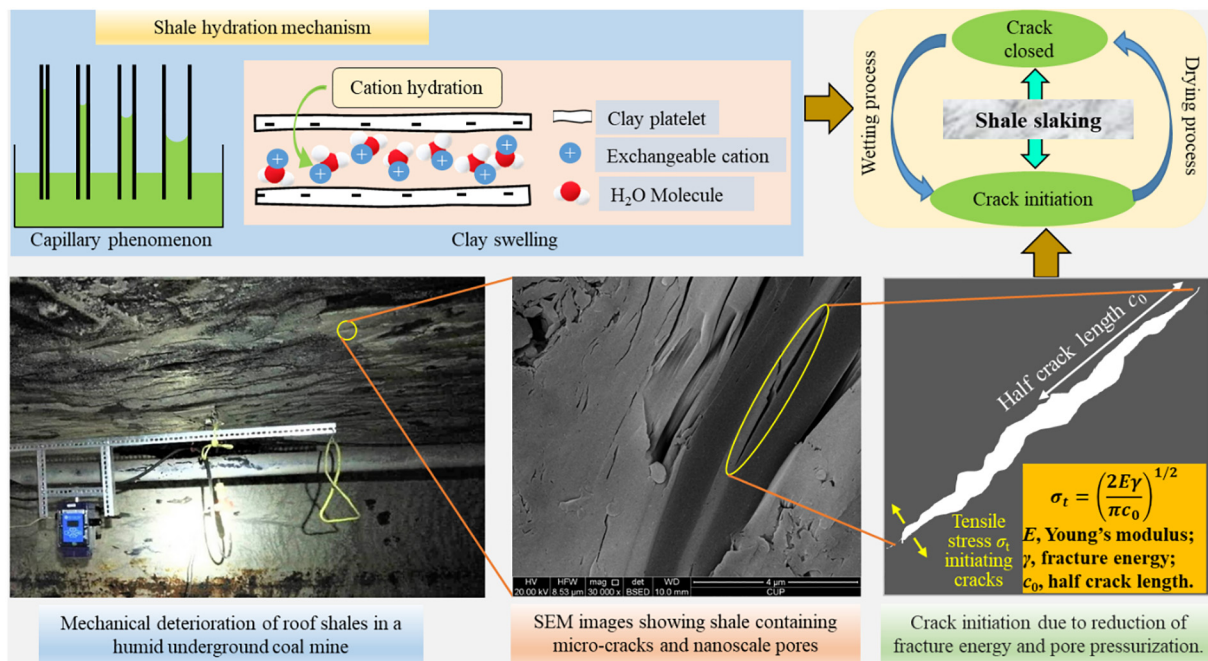


**Fig. 1.** A schematic of moisture-induced mechanical deterioration of roof shales in underground coal mines (the SEM image is from the literature (Wang et al., 2016)). Reduction of fracture energy due to shale hydration can cause the decrease of tensile stress required to initiate microcracks. Shale slaking would occur due to wetting and drying cycles caused by seasonal changes in humidity environment.

and Bajpayee, 2012; Bajpayee et al., 2014; Murphy, 2016). All of these roof failures relate to mine hazards that are either directly or indirectly associated with the mechanical deterioration of roof shales due to seasonal changes in humid environments (Van Eeckhout and Peng, 1975; Aughenbaugh and Bruzewski, 1976).

Water adsorption and retention behavior of the mine roof shale, directly related to the mineralogy and nanopore structure of the shale matrix, is ascribed by either capillary action for shale containing non-expansive clays such as illite and kaolinite (Schmitt et al., 1994; Van Eeckhout and Peng, 1975), or by both capillary and osmotic actions for shale containing expansive smectite (Amorim et al., 2007; Anderson et al., 2010). Generally, shales have high water adsorption capacity due to the relatively high amount of clay minerals with high specific surface area (SSA) (Macht et al., 2011; Hatch et al., 2012) and also have high water retention capacity due to the large number of nano-scale pores (Schmitt et al., 1994; Ferrari et al., 2014). Strength reduction of coal mine roof shales due to water uptake is mainly attributed to several mechanisms including reduction of fracture energy, increases of pore pressure, decrease of capillary tension, chemical deterioration and frictional reduction (Van Eeckhout, 1976). Fig. 1 describes how mechanical deterioration of roof shale occurs under seasonal changes in a humid environment. Roof shales contain micro-cracks and these pre-existing micro-cracks tend to reopen and propagate with the continuous adsorption of water. There are two possible reasons for crack propagation: (1) The tensile stress required to initiate the cracks decreases (Atkinson, 1984) due to the reduction of fracture energy (Van Eeckhout, 1976) with water adsorption; (2) Air entrapment and pore pressurization due to rapid immersion in water can induce tensile stresses (Van Eeckhout, 1976; Schmitt et al., 1994) and dilate the crack tip. Wetting-drying cycles resulting from seasonal changes in humidity can result in the cyclic expansion and contraction of micro-cracks resulting in failure of the micro-skeleton of the shale, manifest as slaking failures (Van Eeckhout, 1976; Poulsen et al., 2014). In addition, water uptake can cause changes in effective stress due to the release of matric suction (Bishop et al. 1960; Bishop and Bjerrum, 1960) and/or induced swelling pressure (Anderson et al., 2010). This may alter the state of stress in shale roof strata, representing another possible factor

implicated in roof failure. The microscopic deterioration of shale combined with changes in the state of stress are directly related to the evolving pore structure of the roof shales and their water adsorption and retention behaviors. Therefore, an improved understanding of pore structure and water adsorption and retention behavior is a key requirement in defining the physical and/or mechanical performance of roof shales under different environmental conditions.

Various techniques have been employed to characterize the pore structure of shale/coal matrix. These include atomic force microscopy (AFM) (Javadpour et al., 2012), field emission scanning electron microscopy (FE-SEM) (Chalmers et al., 2012; Dieterich et al., 2016), nuclear magnetic resonance cryoporometry (NMR-C) (Tong et al., 2017; Zhang et al., 2017a), high-pressure mercury intrusion porosimetry (MIP) and low-pressure gas adsorption (Kuila and Prasad, 2013; Wang et al., 2014, 2016), ultra-/small angle X-ray scattering (USAXS/SAXS) (Zhao et al., 2014), and ultra-/small angle neutron scattering (USANS/SANS) (Mastalerz et al., 2012; Bahadur et al., 2014, 2015; Zhang et al., 2017b). Each technique has its own advantages and disadvantages. Fluid invasion techniques such as low-pressure  $N_2/CO_2$  adsorption, He and Hg porosimetry only provide information of accessible pores where the pore size is larger than that of probing molecule. However, small angle scattering (SAS) techniques, including USAXS/SAXS and USANS/SANS, non-destructively probe both accessible and inaccessible pores ranging in size from nanometers to micrometers (Melnichenko et al., 2012; Ruppert et al., 2013; Zhang et al., 2015). Previous studies show that the pore size distributions (PSD) of shale samples obtained from USANS/SANS are in good agreement with those obtained from low-pressure  $N_2$  adsorption (Clarkson et al., 2013; Sun et al., 2017). Whereas, the PSDs obtained from mercury intrusion porosimetry are offset from those obtained by both SANS and  $N_2$  invasion methods – this is likely due to the pore dilation and skeletal compression resulting from these invasive methods as well as the preferred recovery of pore throat rather than pore body diameters obtained by high-pressure mercury intrusion (Clarkson et al., 2013). Thus, a combination of different techniques may be utilized to potentially provide a more complete understanding of pore structure and morphology than one method in isolation.

Shale matrix exhibits a considerably more complex pore system architecture than other non-organic and indurated sedimentary rocks (e.g. sandstones) since shales have both conventional coarse-grain pores from inorganic minerals such as quartz or carbonate and ultrafine pores from both organic matter (kerogen) and clay minerals. Thus, pore structure characterizations of both Cretaceous shales (using USANS/SANS (Bahadur et al., 2014)) and Northwestern Hunan shales (using combined field emission-scanning electron microscopy (FE-SEM), MIP and gas adsorption (Wang et al., 2014)) show that meso- and micropores dominate the total porosity and SSA of shale rocks. Studies combining low-pressure  $N_2$  adsorption and high-pressure mercury porosimetry indicate that the dominant illite-smectite clays contribute to the volume of micropores and fine mesopores in shales (Kuila and Prasad, 2013). This is because illite-smectite clays exhibit a multiscale pore structure that is associated with spaces between clay-platelet bundles (10–100 nm), interlayer spaces (< 10 nm) and spaces between aggregates (> 10  $\mu$ m) (Aylmore and Quirk, 1967; Clarkson et al., 2013; Kuila and Prasad, 2013).

In this study, we investigate the pore and pore network characteristics and architecture of a single fireclay and four shale samples from coal mines in the Illinois basin using a combination of SANS, low-pressure  $N_2$  adsorption (LPNA) and MIP techniques. The porosity, SSA and fractal dimension as well as distributions of pore volume are directly measured and quantified. Based on the results, detailed overall distributions of pore volume are compared among different techniques. Finally, we link the pore characteristics to pore-water imbibition, adsorption and retention characteristics to explain the behavior of water vapor adsorption for the fireclay and shale samples.

## 2. Experimental work

A series of techniques were applied to probe for an overall understanding of mineralogy, pore structure and water retention/adsorption behavior as shown in Fig. 2. Specifically, the mineralogy was quantified by X-ray diffraction for mineral compositions and total organic carbon (TOC) measured for kerogen content. The pore structure was characterized by combined LPNA, MIP and SANS techniques. Water adsorption isotherms were obtained using a dynamic vapor sorption (DVS) instrument. The water retention behavior was semi-empirically evaluated by the PSD obtained from LPNA and MIP techniques.

### 2.1. Sample collection and total organic carbon

A total of five samples were collected from two Illinois coal mines - Bear Run Mine located at Carlisle, Indiana, and Wildcat Hills Mine located at Equality, Illinois, as shown in Fig. 3. The samples were collected from active mine faces and pits, which were freshly excavated, unweathered and well preserved and at measured temperature and humidity conditions. The sample descriptions are listed in Table 1. The two gray shales (labeled as 6R and 5A) and the fireclay (labeled as 7F) contain negligible TOC compared to that of the two black shales (labeled as 6F and H6). The TOC were measured to be ~31.4% and ~21.4% for 6F and H6, respectively.

### 2.2. X-ray diffraction

Mineralogical compositions by weight fraction were characterized for all five collected samples by X-ray diffraction (XRD) analysis. The raw diffraction data were interpreted by Jade software to determine the mineral contents. The collected samples were pulverized to minus 300 mesh and examined by XRD at the Materials Characterization Laboratory (MCL) at Penn State University. The samples were tested under vacuum and at room temperature. The intensity data were collected over a  $2\theta$  range of 5–70° in increments of 0.02°.

### 2.3. Low-pressure $N_2$ adsorption

$N_2$  ad-/desorption isotherms were measured at 77 K and on powder samples with particle size of 60–80 mesh using a Micromeritics ASAP 2020 apparatus located at Penn State University. To avoid damage of organic matter and to ensure the completion of degassing before the measurements, all five samples were degassed at ~80 °C under vacuum for approximately 16 h prior to the LPNA experiments. The adsorption isotherms were obtained under a wide range of relative pressures ( $p/p_0$ ) from 0.009 to 0.994. The obtained isotherms were interpreted using the standard Brunauer-Emmett-Teller (BET) model to define total surface area and density functional theory (DFT) was used in the quantification of the distribution of pore volume as a function of pore width. Detailed information on the interpretation of the  $N_2$  sorption isotherms is discussed in a previous study (Gregg and Sing, 1982).

### 2.4. Mercury intrusion

The total porosities, SSAs and PSDs of the five samples were

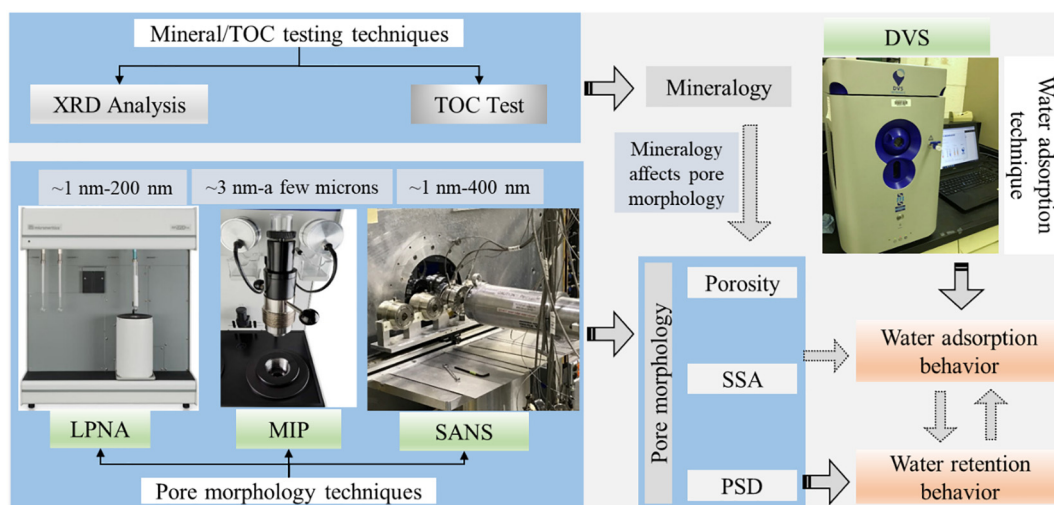


Fig. 2. Technical approaches applied to characterize the mineralogy, pore structure, and water retention/adsorption behaviors. Note: TOC: total organic carbon; XRD: X-ray diffraction; LPNA: low-pressure  $N_2$  adsorption; MIP: mercury intrusion porosimetry; SANS: small-angle neutron scattering; DVS: dynamic vapor sorption system; SSA: specific surface area; PSD: pore size distribution.

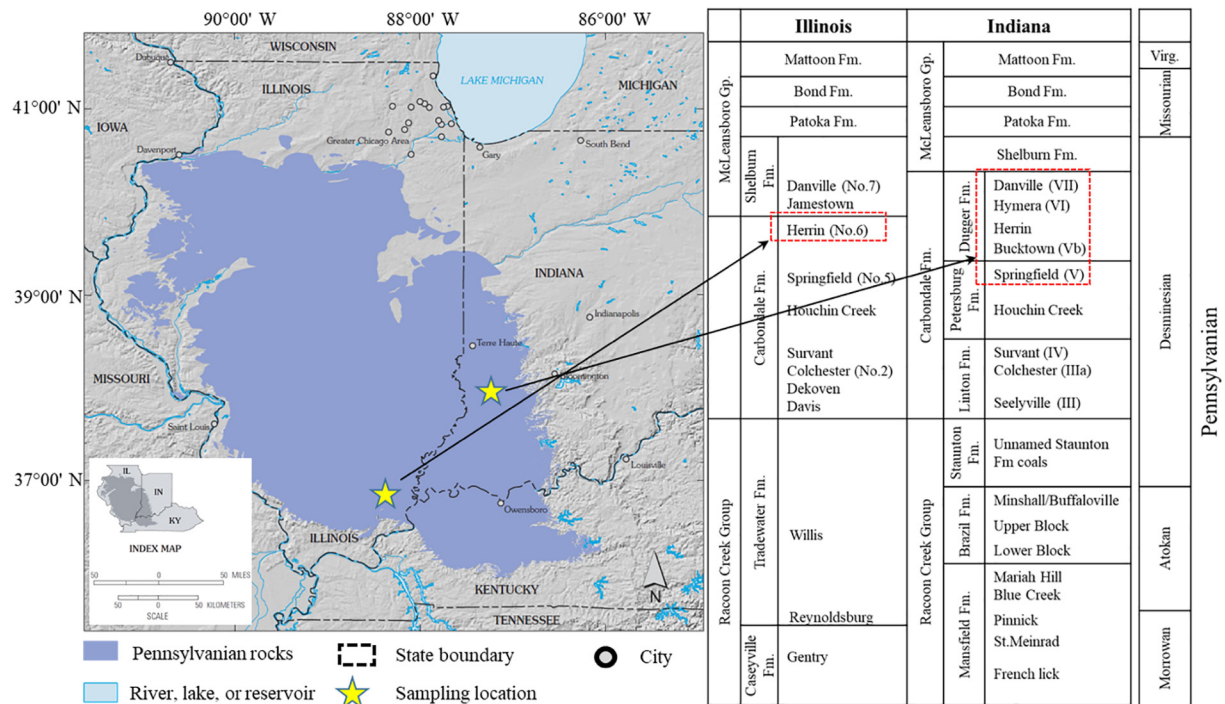


Fig. 3. Sampling locations from coal seams in Illinois basin (map from the literature (Hatch and Affolter, 2002)).

**Table 1**  
Description of the samples from Illinois basin in Pennsylvanian age.

Sample name	Shale type	TOC	Mine name	Location	Coal seam
7F	gray fireclay	0%	Bear Run Mine	Carlisle, Indiana	Danville (No.7)
6R	gray shale	0%	Bear Run Mine		Hymera (No.6)
5A	gray shale	0%	Bear Run Mine		Springfield (No.5A)
6F	black shale	31.4%	Bear Run Mine		Hymera (No.6)
H6	black shale	21.4%	Wildcat Hills Mine	Equality, Illinois	Herrin No.6

obtained from mercury intrusion analysis using a Micrometrics Autopores V 9620 located in the MCL at Penn State University at pressures up to 60,000 psia. Small bulk samples ~0.5–1 cm in dimension were prepared to fit into a 15 cc penetrometer. Total pore volume, SSA and distribution of pore sizes ranging from 3 nm to tens of micrometers were quantified from the pressure versus intrusion/extrusion volume data based on the Washburn equation (Washburn, 1921) given by

$$p = -\frac{2\gamma_m \cos \theta_m}{r} \tag{1}$$

where  $p$  (MPa) is the intrusion/extrusion pressure;  $\gamma_m$  is surface tension of mercury (~0.48 N/m);  $\theta_m$  is contact angle of mercury (~140°);  $r$  ( $\mu\text{m}$ ) is pore radius when mercury enters at pressure  $p$ .

2.5. SANS

SANS experiments were performed on powder samples with grain size of ~ 0.125 mm loaded into the aluminum sample holders with 1.6 mm internal thickness, using the General-purpose small-angle neutron scattering (GP-SANS) instrument at Oak Ridge National Laboratory (ORNL). The sample detector distances were selected as 1.1 m, 8.8 m and 19.2 m to cover a total range of the scattering vector of  $0.001 < Q < 1 \text{ \AA}^{-1}$ , where  $Q = 4\pi\lambda^{-1} \sin(\theta/2)$  and  $\theta$  is the scattering angle. The neutron wavelength  $\lambda$  was set at 4.75 Å for detector distances of 1.1 m and 8.8 m, and was set at 12 Å for a detector distance of 19.2 m. The wavelength spread  $\Delta\lambda/\lambda$  is 13%. Generally, two relationships can be used to determine the pore size from the neutron

data. First, pore size may be estimated from Bragg's law:  $r \approx \pi/Q$ . The other empirical relationship between pore radius  $r$  of a polydisperse porous medium and the scattering vector  $Q$  is:  $r \approx 2.5/Q$  (Radliński et al., 2000). In this study, the later relationship was used to correlate the length scales in the reciprocal and real spaces. Scattered neutrons were detected using a  $1 \times 1 \text{ m}^2$  helium-filled two dimensional (2D) position-sensitive detector with  $192 \times 192$  pixels. The raw 2D data were corrected from the efficiency of the detector pixel, scattering of the empty Al cell, and dark current, which represents the ambient radiation background and electronic noise, and 360° azimuthally averaged to produce the one-dimensional profile, which was obtained using the NCR Igor macros package (Kline, 2006).

2.6. Water vapor adsorption

Water vapor adsorption isotherms were determined on the 60–80 mesh powder samples at 25 °C using the dynamic vapor sorption (DVS) method. The DVS instrument accurately determines the water vapor ad-/desorption isotherms from 0% to ~96% relative humidity (RH) with an adjustable RH step at ~10%. The mass change of the sample due to water vapor ad-/desorption was measured by a microbalance in the DVS system with a sensitivity of  $0.1 \mu\text{g} \pm 1\%$ . The equilibrium criterion is achieved by specifying a rate of mass change  $dm/dt$  to be  $< 0.002\%/min$ . The reproducibility of the laboratory results was guaranteed by performing three repeat experiments for each sample.

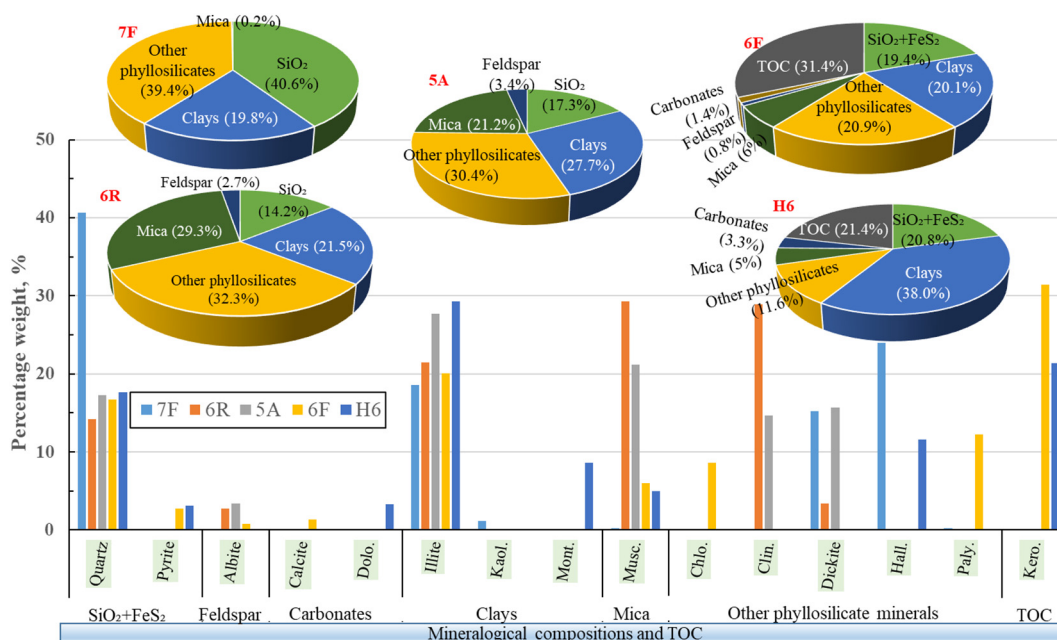


Fig. 4. Weight percentages of mineralogical composition (based on XRD analysis) and/or TOC content of the five samples studied. Note: Dolo. stands for dolomite; Kaol. for kaolinite; Mont. for montmorillonite; Musc. for muscovite; Chlo. for chlorite; Clin. for clinocllore; Hall. for halloysite and Paly. for palygorskite.

### 3. Results and discussion

#### 3.1. Chemical composition by XRD and TOC analyses

The mineralogical composition by weight percentage and TOC content for the five samples are shown in Fig. 4. Overall, the five samples show a broad range of inorganic compositions. The dominant minerals for the five samples are quartz, clays (mainly illite), mica (muscovite) and other phyllosilicate minerals including chlorite, clinocllore, dickite, halloysite, and palygorskite. In particular, the fireclay contains quartz (40.6%), clays (59.4%), mica and other phyllosilicate minerals instead of pyrite, albite and carbonates. The two gray shales (6R and 5A) contain no pyrite and carbonates but contain a small amount of albite at 2.7% and 3.4%, respectively. The two black shales (6F and H6) contain little pyrite, at 2.7% and 3.1%, respectively. Sample 6F contains only 1.4% calcite and the H6 black shale contains a few percent of dolomite (3.3%). Sample H6 contains 8.6% montmorillonite and the highest proportion of illite (29.3%) among the samples tested. We find a remarkable difference in TOC content between the two black shales (6F and H6) and the three other samples – the fireclay (7F) and the two gray shales (6R and 5A). The 6F and H6 black shales have significantly high TOC contents at 31.4% and 21.4%, respectively, whereas there are negligible amounts in the fireclay (7F) and gray shales (6R and 5A). These mineral components and TOC contents will be used to calculate the scattering length density (SLD) of each sample for the SANS analysis (section 3.4).

#### 3.2. Low-pressure $N_2$ adsorption analysis

Low-pressure  $N_2$  ad/de-sorption isotherms at 77 K together with their hysteric patterns can be used to characterize pore shape and pore structure across the spectrum from micro- to macro-pore. The ad/de-sorption isotherms for the five tested samples are shown in Fig. 5. According to the IUPAC classification, all the samples exhibit an H3-type hysteresis loop suggesting the process of capillary condensation and evaporation within the mesopores – further suggesting that those shale samples primarily contain slit-shaped pores (Gregg and Sing, 1982). Micropores in certain clay minerals may be associated with slit-shaped pores (Quirk and Aylmore, 1971; Kuila and Prasad, 2013).

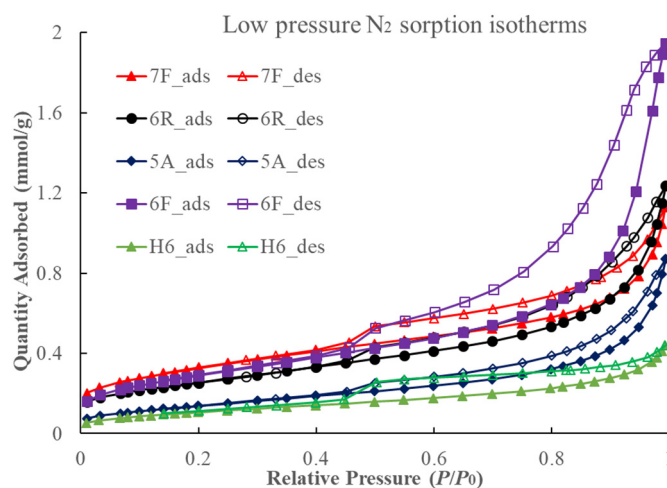


Fig. 5. Low-pressure  $N_2$  ad/de-sorption isotherms for the studied five samples at 77 K.

Another observation of the hysteric patterns of the five tested samples is the sudden closure of the adsorption and desorption branches at a  $p/p_0$  of  $\sim 0.45-0.5$ , referred to as the ‘Tensile Strength Effect’ (Groen et al., 2003). This is attributed to the collapse of the hemispherical meniscus during capillary evaporation in pores with a size of approximately 4 nm and defines the lower limit of the pore size evaluated from the desorption branch as  $\sim 4-5$  nm. Therefore, we used the adsorption branch, rather than desorption branch, to recover the pore size characteristics based on DFT theory, in this study.

Results of surface area, pore volume and porosity estimated by low-pressure  $N_2$  adsorption are listed in Table 2. The 7F fireclay exhibits the highest BET surface area (26.23  $m^2/g$ ). The two black shales (6F black shale at 31.4% TOC) have a relatively high surface area (23.67  $m^2/g$ ) while sample H6 (21.4% TOC) has the smallest surface area (8.88  $m^2/g$ ). Despite the larger BET surface area, the 7F fireclay exhibits a smaller total surface area than that of 6F black shale, based on the DFT calculation. This is consistent with the  $N_2$  adsorption isotherms that show that the 7F fireclay has a larger adsorbed mass at  $p/p_0 < 0.35$  where

**Table 2**  
Pore volume, surface area, and porosity from N<sub>2</sub> adsorption<sup>a</sup>.

Shale sample	BET SA, m <sup>2</sup> /g	Total pore volume <sup>b</sup> , cm <sup>3</sup> /g	Total SA <sup>c</sup> , m <sup>2</sup> /g	Hg bulk density, g/cm <sup>3</sup>	Total porosity <sup>b</sup> , %
7F	26.23	0.0201	10.15	2.487	5.0
6R	20.64	0.0254	9.37	2.491	6.3
5A	11.49	0.0154	6.43	2.456	3.8
6F	23.67	0.0488	12.48	1.680	8.2
H6	8.88	0.0139	3.86	1.805	2.5

<sup>a</sup> Pore volume, surface area (SA) and average pore size are obtained based on DFT theory.

<sup>b</sup> Total volume in pores < 200 nm.

<sup>c</sup> Total surface area in pores larger than 1.5 nm.

the BET model is applied to evaluate the surface area. Conversely, DFT theory considers the overall quantity of adsorbed N<sub>2</sub> to evaluate the total surface area where the N<sub>2</sub> adsorption capacity of the 7F fireclay is smaller than that of the 6F black shale at larger  $p/p_0$  (> 0.7). Combining with the bulk density obtained from mercury intrusion porosimetry, the N<sub>2</sub> porosity can be estimated from the product of total pore volume and bulk density shown in Table 2. The results show that the 6F black shale has the highest (8.2%) and H6 has the lowest porosity (2.5%), with an average porosity of all samples of 5.1%.

Pore size distributions (PSD) can be presented as cumulative, incremental, or differential distribution curves (Mastalerz et al., 2012; Kuila and Prasad, 2013; Clarkson et al., 2013). The incremental pore volume with respect to pore width for the studied shale samples (Fig. 6) were obtained from DFT, which show bimodal distributions of pore volume (peaks at ~3 nm and ~25 nm). The 6F black shale exhibits a larger pore volume for pore sizes in the range 10 nm to 100 nm than the other shale samples. The 7F fireclay has a greater pore volume at a smaller pore size range between 2 nm and 4 nm among the tested samples. Reorganization of pore volume based on the classification of micropores (1.5–2 nm), mesopores (2–50 nm) and macropores (50–200 nm) over the experimental pore range for the five samples are shown in Fig. 7. Mesopores predominantly contribute to the total pore volumes (65–82%). Micropores (1.5–2 nm) for the 7F fireclay, 6R gray shale, 6F and H6 black shales account for ~5–22% of total pore volume. Since the probing size of N<sub>2</sub> sorption based on DFT theory is limited to ~1.5 nm and 200 nm, smaller micropores (< 1.5 nm) and larger macropores (> 200 nm) were not classified in this study.

### 3.3. Mercury intrusion analysis

Mercury is a strongly non-wetting fluid (high contact angle) and will not spontaneously penetrate into pores of a porous medium by capillary

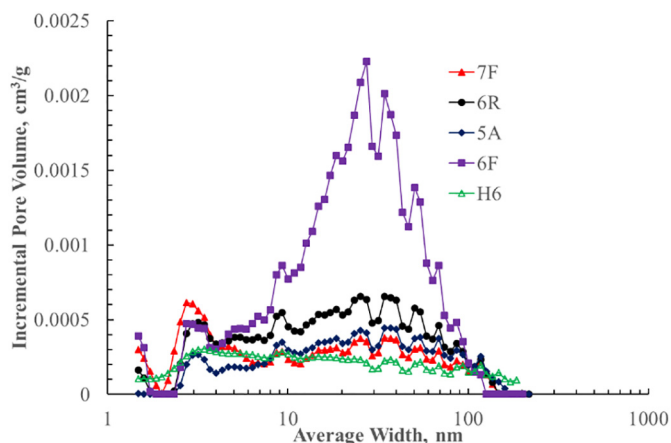


Fig. 6. Distributions of pore volume for the studied five samples.

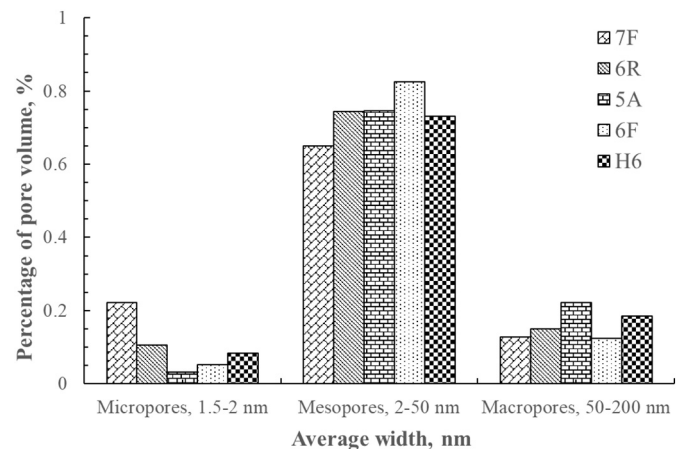


Fig. 7. Percentages of pore volume based on the classification of micropore, mesopore, and macropore for the studied five samples.

action. Mercury intrusion porosimetry (MIP) drives mercury into pores under the action of external pressure with the pore size distribution recovered from the Washburn equation (Washburn, 1921). The liquid pressure required to intrude into the pores is inversely proportional to the size of the pores. Apart from requiring the assumption of cylindrical pores, MIP only quantitatively detects pore throat sizes, the entrance to a pore, rather than the pore body diameter itself (Giesche, 2006). The intrusion and extrusion curves for the five samples are shown in Fig. 8. The 6F black shale exhibits the highest volume of mercury intruded at high pressures, up to ~60,000 psia, suggesting the largest cumulative pore volume (> ~3 nm) for sample 6F, while the H6 black shale presents the lowest cumulative pore volume (> ~3 nm). The 7F fireclay and the two gray shales (6R and 5A) have similar intrusion volumes. This is consistent with the low-pressure N<sub>2</sub> adsorption measurements described in the previous section.

A hysteresis is clearly apparent between mercury intrusion and extrusion processes (Fig. 8). There are two possible explanations. First, it may be due to the change in contact angle of mercury between the intruding and extruding menisci (Lowell, 1980; Lowell and Shields, 1984). However, thermodynamic arguments for contact-angle hysteresis are difficult to justify and inadequate to explain the phenomena in porosimetry (Conner et al., 1984). Rather, structural hysteresis may be expected to occur where the pressures for intrusion and extrusion processes are controlled by different aspects of the pore structure. For example, for ‘ink-bottle’ pores consisting of large pore bodies with narrow pore necks, intrusion is controlled by the size of pore throat, whereas extrusion is controlled by the size of pore body (Conner et al.,

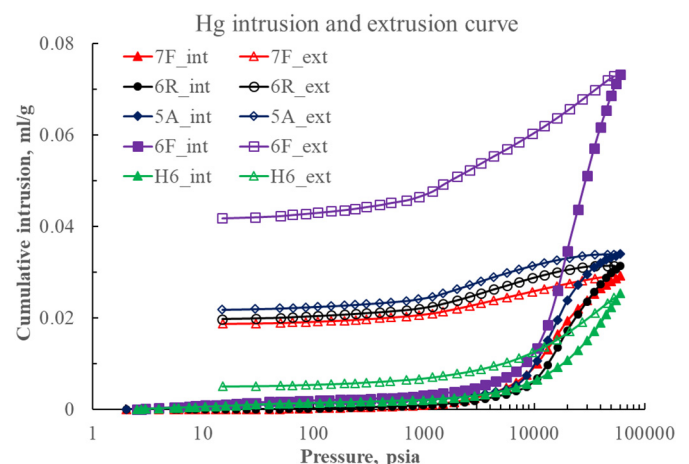


Fig. 8. Mercury intrusion and extrusion curves for the studied five samples.

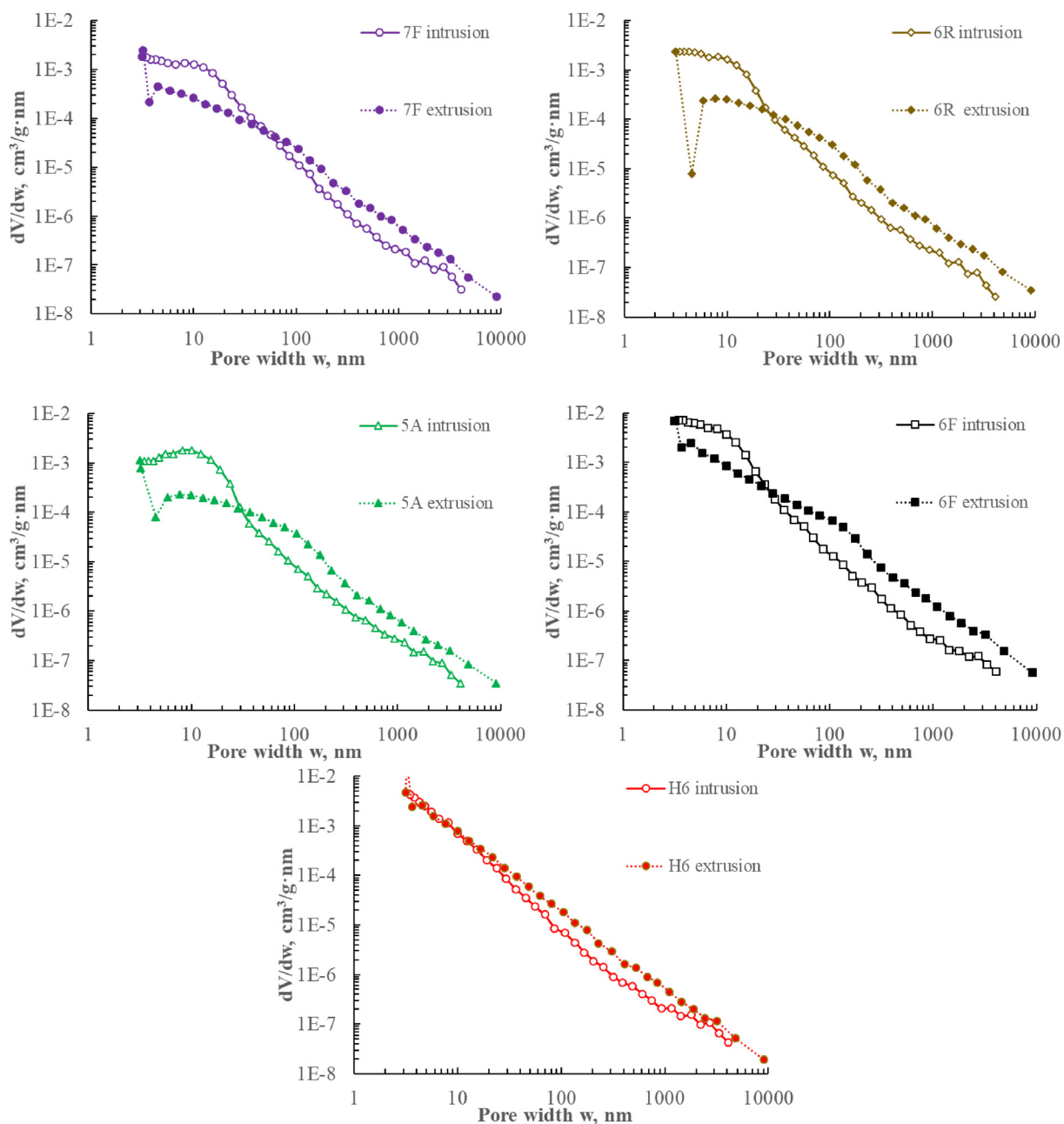


Fig. 9. PSDs by mercury intrusion and extrusion data for the studied five samples.

**Table 3**  
Pore volume, surface area, and porosity from MIP.

Shale sample	Skeletal density, g/cm <sup>3</sup>	Bulk density, g/cm <sup>3</sup>	Total pore volume, cm <sup>3</sup> /g	Total porosity, %	Total SSA, m <sup>2</sup> /g	Percent of mesopore <sup>a</sup> volume, %	Percent of macropore <sup>b</sup> volume, %
7F	2.682	2.487	0.0292	7.26	11.71	88.3	11.7
6R	2.702	2.491	0.0313	7.80	14.87	92.1	7.9
5A	2.679	2.456	0.0339	8.33	12.62	89.4	10.6
6F	1.915	1.680	0.0732	12.30	38.09	92.2	7.8
H6	1.892	1.805	0.0253	4.57	14.36	86.4	13.6

<sup>a</sup> Mesopores between 3 nm and 50 nm.

<sup>b</sup> Macropores larger than 50 nm.

1984; Wardlaw et al., 1988). Furthermore, Conner et al. (Conner et al., 1986) compared PSDs of the compressed aerosols measured by both mercury (Hg) porosimetry and low-pressure N<sub>2</sub> adsorption. It was concluded that pore information extracted by mercury intrusion process

corresponds to N<sub>2</sub> desorption process, characterizing the constrictions within the void network – the pore throats in this particular case. However, mercury extrusion process and N<sub>2</sub> adsorption process are in agreement for pore structure characterization, determining the openings

within the void network – the pore bodies in this particular case. The PSDs for the five samples recovered by both intrusion and extrusion data are shown in Fig. 9. The volume distribution curves are recovered by taking the derivative of the volume intruded (or extruded) with respect to the diameter of intrusion (or extrusion). The overall trends of the PSDs for the five samples are similar. The difference in PSDs obtained from the intrusion and extrusion processes for the five samples could be due to structural hysteresis. From Fig. 9, despite the limitation in detecting micropores, mercury intrusion/extrusion is applicable over a wide range of pore sizes up to tens of micrometers.

Results of surface area, pore volume and porosity estimated by mercury porosimetry are shown in Table 3. The 6F black shale exhibits the highest mercury porosity (12.3%) and SSA (38.09 m<sup>2</sup>/g), while the H6 black shale has the lowest mercury porosity (4.57%) and SSA (14.36 m<sup>2</sup>/g). This is consistent with the results from the N<sub>2</sub> adsorption data. The 7F fireclay and 6R and 5A gray shales exhibit comparable mercury intrusion porosities and SSAs with average values of 7.8% and 13.07 m<sup>2</sup>/g, respectively. The mercury porosities and SSAs are greater than the N<sub>2</sub> porosities and SSAs recovered from DFT theory. This may be caused by the different probing length scales between mercury intrusion and low-pressure N<sub>2</sub> adsorption. This could also result from the influence of high pressure intrusion on grain compression and/or crushing of the pore walls and the opening of closed pores (Bustin et al., 2008; Clarkson et al., 2013). The percentages of mesopores (3–50 nm) and macropores (> 50 nm) in terms of pore volume are listed in Table 3. Compared to N<sub>2</sub> adsorption results, mesopores contribute to the MIP measured total pore volumes even more predominantly, indicating that the possible opening of closed pores due to high pressure intrusion mainly occurs in the mesopore range.

### 3.4. SANS analysis

The SLD of a multicomponent system may be estimated by a weighted average of volume over all components including both minerals and TOC (Bahadur et al., 2014). The weight percentage of mineralogical components and TOC of the five samples (Fig. 4) were determined by XRD analysis and TOC measurements, respectively, while the volume fraction of each component were calculated on the basis of respective density. The SLD of each component including mineral and TOC for the five samples is calculated according to (Radlinski et al., 1996):

$$\rho_n = \frac{N_A d}{M} \sum_j p_j \left( \sum_i s_i b_i \right) \quad (2)$$

where  $N_A$  is Avogadro's number ( $6.022 \times 10^{23}$ ),  $d$  is the physical density,  $s_i$  is the proportion by number of nucleus  $i$  in compound  $j$ ,  $p_j$  is the proportion by molecular number of the compound  $j$  in the mixture, and  $b_i$  is the coherent scattering amplitude for the nucleus  $i$ . The calculated SLDs of the five samples are shown in Table 4.

Fig. 10 shows the SANS profiles for the five shale samples under ambient conditions. The scattering curves follow a power law over a range of  $Q$  from  $\sim 0.001 \text{ \AA}^{-1}$  to  $\sim 0.1 \text{ \AA}^{-1}$ . This may be represented in log-log scale by straight lines with slopes close to  $-3$ , indicating self-

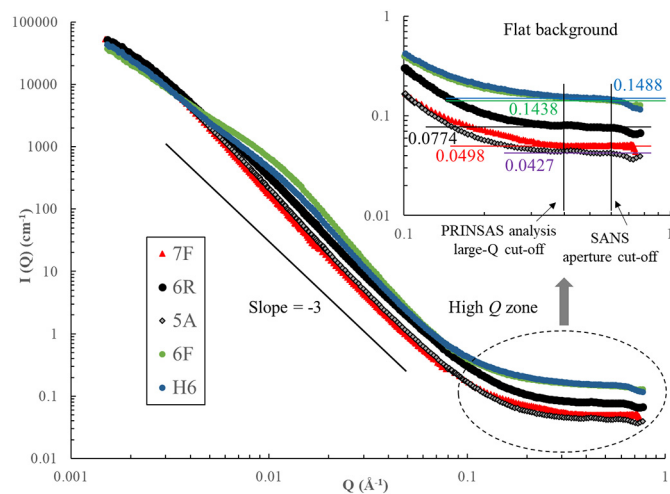


Fig. 10. SANS profiles of studied Illinois roof shales. The flat background, SANS aperture cutoff and PDSP model cutoff are indicated for each shale.

similarity of the pore space (Radliński et al., 2000). Note that the deviation of scattering intensity from power law scattering at  $Q$  smaller than  $\sim 0.003 \text{ \AA}^{-1}$  (Fig. 10) could be caused by the multiple scattering effect due to a relatively long neutron wavelength (12 Å) (Radliński et al., 1999). Besides, it is apparent that the scattering curves have flat backgrounds at high  $Q$  values larger than  $0.1 \text{ \AA}^{-1}$  which may have two possible sources. One is due to the scattering from micropores in the shale matrix. The other is  $Q$ -independent scattering background arising from the incoherent scattering of hydrogen atoms in the organic matter and/or the residual moisture in the shale pores (Radlinski and Radlinska, 1999; Mastalerz et al., 2012; Ruppert et al., 2013). The flat backgrounds are shown in Fig. 10. The two black shales (6F and H6) have higher backgrounds which are mainly due to their remarkably high content of organic matter. The 6R gray shale has a slightly higher flat background than that of 7F fireclay and 5A gray shale, which may result from the 6R gray shale exhibiting a higher degree of micro-scale inhomogeneities or higher content of native water bound within the clay minerals.

The polydisperse spherical pore (PDSP) model (Radlinski et al., 2004), as implemented in the PRINSAS software (Hinde, 2004), was used to analyze the background-subtracted SANS data:

$$I(Q) = N(\Delta\rho^*)^2 \int V^2(r)f(r)P(Q,r)dr \quad (3)$$

where  $N$  is the pore number density;  $(\Delta\rho^*)^2$  is the scattering contrast between rock matrix and pore, which is equal to  $(\rho_s^* - \rho_p^*)^2$ ; where  $\rho_s^*$  and  $\rho_p^*$  are the SLD of the solid matrix and pore, respectively;  $V(r)$  is the spherical volume;  $r$  is the spherical radius;  $f(r)$  is the fractal size distribution; and  $P(Q,r)$  is the spherical form factor. Porosities and SSAs were obtained from the fitting of the PDSP model to the experimental scattering data using the volume-averaged SLD for the five studied samples shown in Table 4. The total porosity of the shale samples can also be evaluated by the model-independent Porod invariant (PI)

Table 4  
Porosity and surface area from SANS<sup>a</sup>.

Shale #	SLD, $\times 10^{10} \text{ cm}^{-2}$	Porod Invariant porosity, %	PDSP porosity (%)	SSA <sup>b</sup> , $\text{cm}^2/\text{cm}^3$	Hg density, $\text{g}/\text{cm}^3$	SSA, $\text{m}^2/\text{g}$
7F	3.63	3.7	4.0	3.177E+05	2.487	12.77
6R	3.65	5.9	6.2	5.376E+05	2.491	21.58
5A	3.62	3.8	4.1	2.659E+05	2.4561	10.83
6F	3.87	8.0	8.8	3.406E+06	1.6795	20.28
H6	3.84	7.9	8.0	4.844E+05	1.8051	26.8

<sup>a</sup> Flat background was subtracted from SANS data with upper cutoff being  $\sim 0.4 \text{ \AA}^{-1}$ .

<sup>b</sup> The probe size for SSA of 7F, 6R and 5A is 6.3 Å; The probe size for SSA of the two black shale 6F and H6 is 7.9 Å.

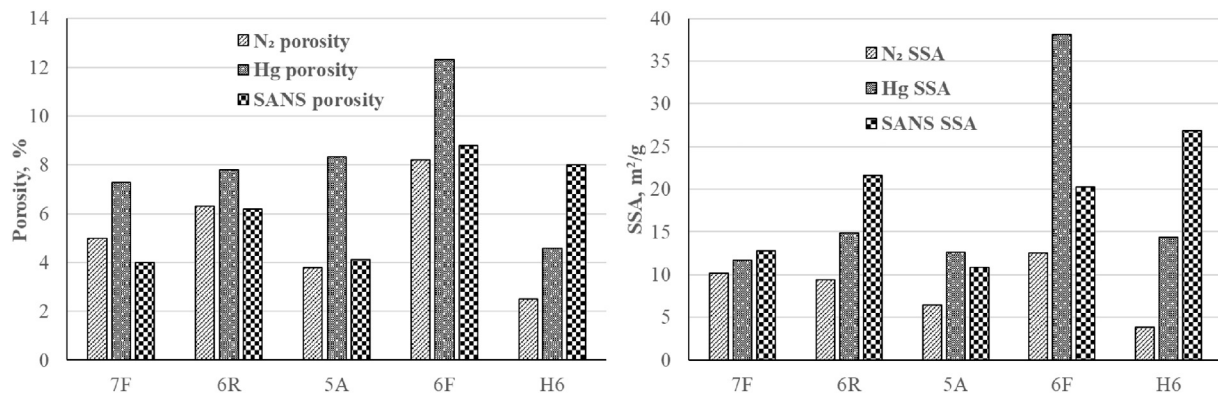


Fig. 11. Porosities and SSAs measured by N<sub>2</sub> adsorption, SANS and Hg intrusion for the studied five samples.

method. For a two-phase system, the Porod invariant can be expressed as:

$$Q_{inv} = \int_0^{\infty} Q^2 I(Q) dQ = 2\pi^2 (\Delta\rho)^2 \phi (1 - \phi) \quad (4)$$

where  $Q_{inv}$  is the model-independent Porod invariant,  $I(Q)$  the scattering intensity ( $\text{cm}^{-1}$ ), and  $\phi$  is the porosity. As shown in Table 4, porosities of the five samples obtained by the PDSP model and PI method match remarkably well with each other. Based on the PDSP model, the SSA of the studied samples are also shown in Table 4.

Fig. 11 shows the porosities and SSAs measured by N<sub>2</sub> adsorption, Hg porosimetry and SANS analysis for the tested samples. PDSP porosities agree well with the N<sub>2</sub> porosities for all the samples except H6 black shale, which exhibits a much higher PDSP porosity (8%) than either its N<sub>2</sub> porosity (2.5%) or Hg porosity (4.6%). The overall SANS SSAs for the samples are larger than the N<sub>2</sub> SSAs. Since the probe sizes for porosity and SSA by the two methods are similar (~1.5 nm for N<sub>2</sub> and ~1.6 nm for PDSP), the overestimation of porosity/SSA by the SANS analysis could be attributed to the fact that SANS technique measures both accessible pores and inaccessible pores that could not be probed by N<sub>2</sub> molecules. For the H6 black shale with much larger porosity and SSA recovered from the SANS analysis, the presence of monomorphonite could be the cause of inaccessible interlayer spaces which cannot be detected by fluid penetration methods (Aylmore and Quirk, 1967). Overall, porosity and SSA for the studied samples based on SANS analysis and mercury intrusion are larger than those of N<sub>2</sub> adsorption because SANS can see through inaccessible pores while high pressure mercury intrusion may crush pore walls, enlarge pore volumes and open closed pores.

### 3.5. Comparison of PSDs among techniques

Distributions of pore volume (Fig. 12) for the five samples obtained by the three techniques agree well with each other over a wide range of pore sizes (~1–100 nm). For H6 black shale, pore volume over the whole range of pore size based on N<sub>2</sub> adsorption presents smaller values compared to the SANS result. This is partially because inaccessible pores are likely present in the shales and vary over a large range of pore sizes - as is suggested by previous USANS/SANS studies (Mastalerz et al., 2012; Clarkson et al., 2013; Ruppert et al., 2013). Moreover, the presence of montmorillonite in the H6 shale could contain negligible internal pore spaces. This internal spaces, which is inaccessible to N<sub>2</sub> molecules, have also been validated by other techniques such as water and/or ethylene glycol adsorption (Newman, 1983), glycerol retention (Diamond and Kinter, 1958), atomic force microscopy (AFM) and ethylene glycol monomethyl ether (EGME) adsorption (Macht et al., 2011). As expected, differential distributions of pore volume of the H6 black shale estimated by SANS are obviously higher than those estimated by N<sub>2</sub> adsorption over the entire range of pore sizes due to the

presence of 8.6% montmorillonite in this sample. It is noted that the PSDs recovered from mercury porosimetry are calculated from the Hg extrusion data, reflecting the information of the pore bodies rather than pore throats (Conner et al., 1984, 1986; Wardlaw et al., 1988).

### 3.6. Water vapor adsorption

Water vapor adsorption isotherms at 25 °C for the five samples are shown in Fig. 13. The isotherms are of Type II according to the classification proposed by Brunauer, Deming, Deming and Teller (Brunauer et al., 1940). The 7F fireclay exhibits the highest capacity for water adsorption (3.3 mmol/g) while the 5A gray shale has the lowest (1.8 mmol/g) at a relative humidity (RH) near 100%. Compared to the 7F fireclay, the 6R gray shale and the 6F black shale have an overall lower capacity for water adsorption when the RH is smaller than 60%, but the capacity sharply increases with increasing RH above this. This is consistent with the pore structure observed by the three techniques (Fig. 11) that the 6R and 6F shales have larger pore volumes/porosities than the 7F fireclay which can provide the main sites for water condensation at high RH. Compared to the 6F black shale and the 6R gray shale, the H6 black shale exhibits a higher water adsorption at RH < 70% but a lower capacity of water adsorption at RH > 85%. This could be attributed to the presence of expansive montmorillonite (8.6%), providing a larger internal SSA as is indicated by N<sub>2</sub> adsorption and SANS analysis for water adsorption at RH < 70%, while water vapor condensation at RH > 85% can be limited due to its smaller external pore spaces as is measured by N<sub>2</sub> adsorption (Fig. 11).

Fig. 14 exhibits positive correlations between total capacity of water adsorption and N<sub>2</sub> porosity and SSA. Despite the intermediate total pore volume recovered from N<sub>2</sub> adsorption, the 7F fireclay exhibits the highest total water capacity at RH ~96% due to the largest SSA for the sample. Therefore, both porosity and SSA influence water adsorption behavior of shale. Based on previous studies (Thommes et al., 2013; Seemann et al., 2017), water adsorption behavior is mainly controlled by pore surface chemistry at low RH values and by pore structure at high RH values where capillary condensation dominates. The effect of both pore structure and surface chemistry on water adsorption behavior of shale will be investigated in the future.

### 3.7. Water retention curve

The deterioration of coal mine roof shales associated with numerous ground control problems depends significantly upon the water retention capacity as previously described. The capillary potential, also called matric suction, is one significant reason for the high water retention in shale matrix containing a large fraction of nanoscale pores (Schmitt et al., 1994). Matric suction in pores smaller than 0.1 μm is much larger than osmotic suction (Mitchell, 1962). Water retention curves for these shale samples, defined as the evolution of matrix

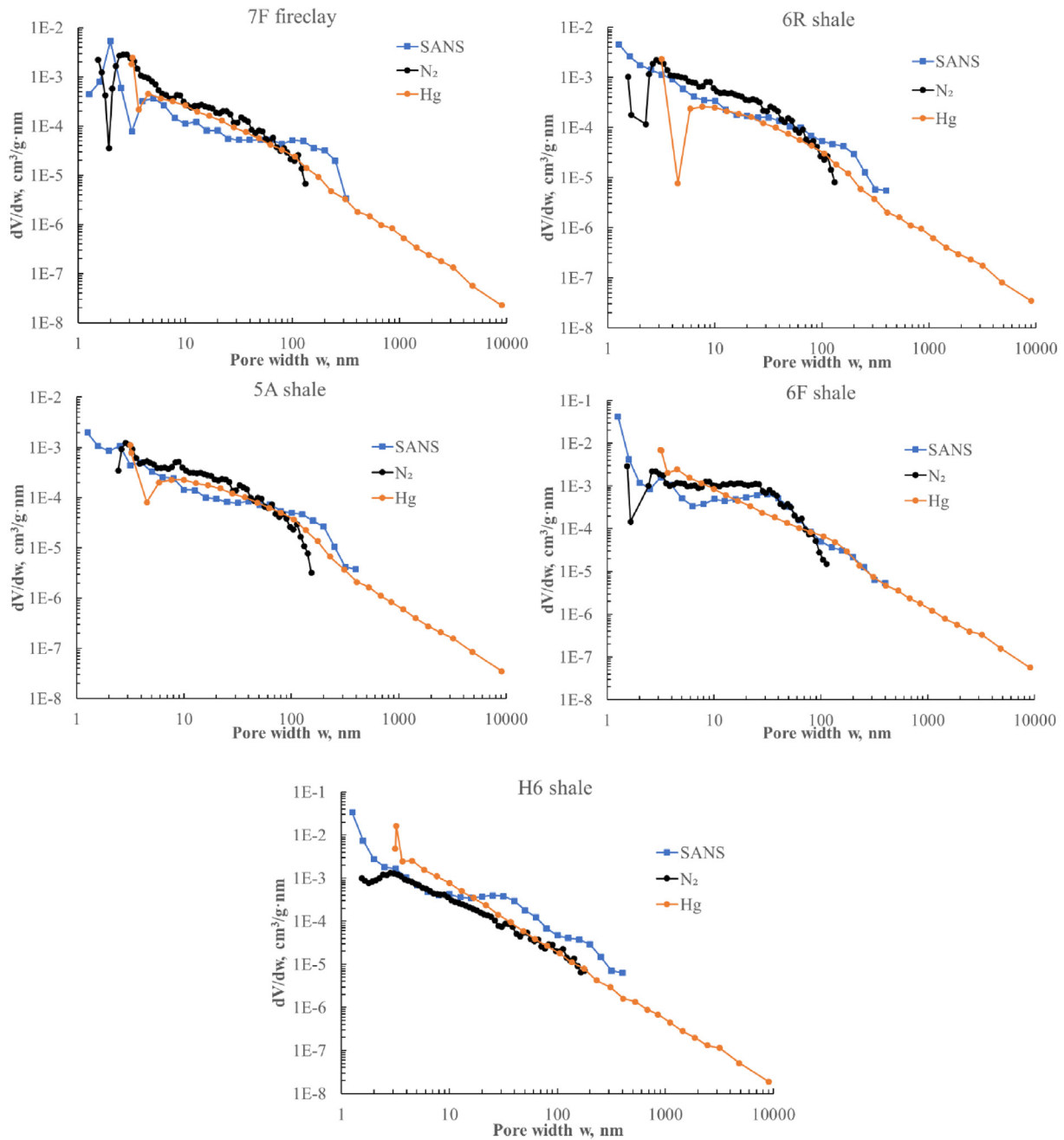


Fig. 12. Comparison of pore volume distributions obtained from N<sub>2</sub> adsorption, SANS and Hg intrusion for the studied five samples.

suction  $\psi_m$  with water saturation/content, have been developed based on the pore size distributions recovered from the combination of N<sub>2</sub> adsorption and mercury porosimetry analyses. Here we assume that the porosities of the shale samples remain constant during the process of water retention, which is reasonable for shales containing negligible proportions of expansive clays. Water retention curves for these five samples are expressed as variations in matric suction with respect to the degree of water saturation. According to the well-known Laplace equation (Powles, 1985), the relation between matric suction  $\psi_m$  and pore radius  $r$  can be expressed as:

$$\psi_m = \frac{2\gamma \cos \theta}{r} \quad (5)$$

where  $\gamma$  is the interfacial tension between air and water ( $72.75 \times 10^{-3}$  N/m) and  $\theta$  is the contact angle between water interface and the shale matrix surface (in this case,  $\theta = 0$ , representing fully

wetting condition).

The saturation of the five samples, defined as the volume of filled pores up to a given pore radius  $r$  divided by the total pore volume  $V_t$  (Schmitt et al., 1994), can be expressed as:

$$S = \frac{1}{V_t} \int_{r_{min}}^r \frac{dV}{dr} dr \quad (6)$$

where  $dV/dr$  is the differential distribution of pore volume over a wide range of pore size from  $\sim 1.5$  nm to tens of micrometers, obtained from the combination of N<sub>2</sub> adsorption and mercury porosimetry analyses.

Fig. 15 describes the water retention curves for the five samples. Matric suctions for the 7F fireclay, 6R and 5A gray shale and 6F and H6 black shales reach to  $\sim 100$ – $150$  MPa for water saturations less than  $\sim 3\%$ . This is much greater than that for sandstones ( $\sim 10$  MPa) (Schmitt et al., 1994). According to Eq. (5), smaller pores tend to have higher water retention capacity. Therefore, samples with a larger proportion of

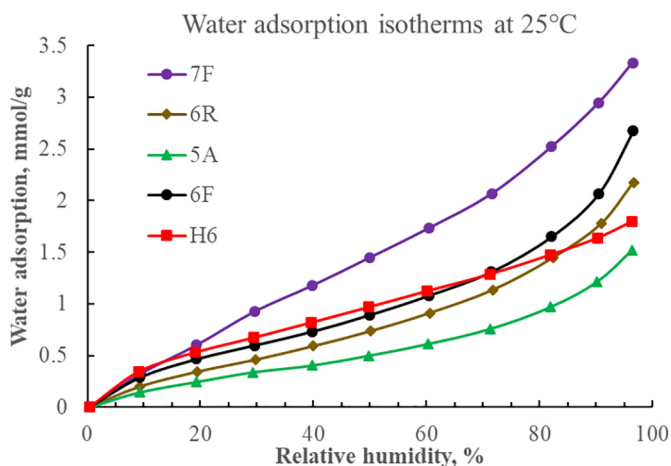


Fig. 13. Water adsorption isotherms for the studied five samples.

micro/meso-pores result in a much larger retention capacity of water than that in sandstones. Additionally, suctions for the tested samples remain fairly high (~2–5 MPa) even for saturations as high as ~80%.

Among the five samples, the 7F fireclay presents the overall largest matric suction with 5A exhibiting a relatively low suction over the large range of water saturations, suggesting a stronger water retention for the 7F fireclay and weaker water retention for the 5A shale. This can be attributed to a larger proportion of micropores (1.2–1.5 nm) in the 7F fireclay and smaller proportion in the 5A shale, as is shown in Fig. 7. The 6F black shale exhibits a relatively low matric suction at low water saturations ( $S < 0.4$ ) but the highest suction at high saturation ( $S > 0.7$ ). Compared to the 6F black shale and 6R gray shale, the H6 black shale exhibits a higher suction at  $S < 0.6$  but a lower suction at  $S > 0.6$ . This is consistent with the amount of water adsorption under different RH values for the five samples as shown in Fig. 13. Intuitively, suction corresponds to water retention capacity while total porosity/SSA determines total amount of water adsorbed. However, the combination of water adsorption isotherms (Fig. 13) and water retention curves (Fig. 15) indicates that samples with higher retention capacity tend to also adsorb more water. Both water retention and adsorption behaviors are mechanistically related to pore structure. However, pore surface chemistry, apart from pore structure, could also play an important role in determining water adsorption behavior at low RH (Thommes et al., 2013; Seemann et al., 2017). Further study should be considered to investigate the effect of pore surface chemistry on water adsorption behavior.

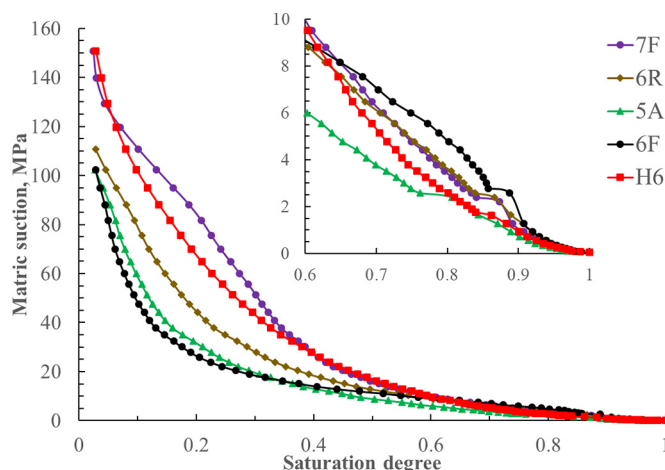


Fig. 15. Water retention curves based on the PSDs obtained by N<sub>2</sub> adsorption and MIP techniques.

#### 4. Conclusions

In this study, nanoscale pore structure characteristics of one fireclay and four shale samples were measured by SANS, N<sub>2</sub> adsorption and MIP techniques. Water vapor adsorption was investigated using a dynamic sorption technique. Pore-water retention characteristics, were semi-empirically evaluated based on differential pore volume distribution determined by both N<sub>2</sub> adsorption and MIP. The conclusions of this study are:

- (1) Distributions of pore volume obtained from SANS, low-pressure N<sub>2</sub> adsorption, and MIP techniques are in agreement over a range of pore sizes from ~1 nm to hundreds of nanometers. Micro/mesopores predominantly contribute to the total pore volume for the studied fireclay and shales.
- (2) SANS porosities are in good agreement with N<sub>2</sub> measured porosities for the 7F fireclay, 6R gray shale, 5A gray shale, and 6F black shale. However, SANS overestimates porosity compared to N<sub>2</sub> adsorption for the H6 black shale – this can be attributed to the internal pores contained in montmorillonite which are inaccessible to N<sub>2</sub> molecules.
- (3) The overestimated porosities from the mercury intrusion data may result from the opening of closed mesopores due to the high pressures necessarily applied during mercury intrusion. Hysteresis observed between mercury intrusion and extrusion processes is likely due to structural effects where the intrusion process is controlled by the size of pore throat and extrusion is controlled by the size of pore

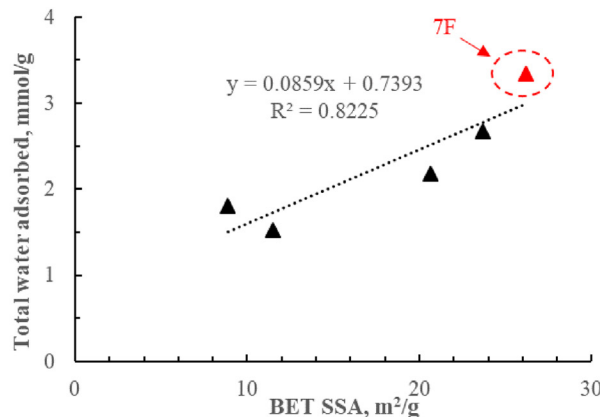
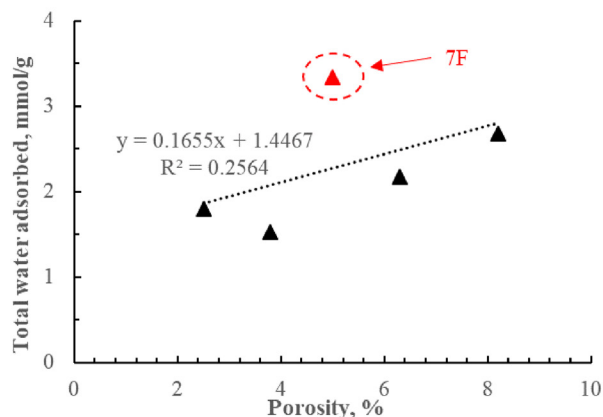


Fig. 14. Correlations between the total capacity of water adsorption and N<sub>2</sub> porosity (left) and SSA (right).

body.

- (4) Pore structures of the five studied samples have a significant impact on their water adsorption and retention behaviors. Water adsorption capacity has a positive correlation with total porosity/SSA, while a large proportion of micro/meso-pores result in strong water retention capacity. Among these five studied fireclay/shales, samples with higher retention capacity tend to adsorb more water.

## Acknowledgement

This work was financially supported by The National Institute of Occupational Safety and Health (NIOSH) under the contract No. NIOSH-200-2016-90385.

## References

- Amorim, C., Lopes, R., Barroso, R., Queiroz, J., Alves, D., Perez, C., Schelin, H., 2007. Effect of clay–water interactions on clay swelling by X-ray diffraction. *Nuclear Instrum. Methods Phys. Res. Sect. A* 580, 768–770.
- Anderson, R., Ratcliffe, I., Greenwell, H., Williams, P., Cliffe, S., Coveney, P., 2010. Clay swelling—a challenge in the oilfield. *Earth Sci. Rev.* 98, 201–216.
- Atkinson, B.K., 1984. Subcritical crack growth in geological materials. *J. Geophys. Res.* 89, 4077–4114.
- Aughenbaugh, N., Bruzewski, R., 1976. Humidity effects on coal mine roof stability. In: US Bureau of Mines Open-File Report, pp. 5–78 (164 pp).
- Aylmore, L., Quirk, J., 1967. The micropore size distributions of clay mineral systems. *Eur. J. Soil Sci.* 18, 1–17.
- Bahadur, J., Melnichenko, Y., Mastalerz, M., Furmann, A., Clarkson, C.R., 2014. Hierarchical pore morphology of cretaceous shale: a small-angle neutron scattering and ultrasmall-angle neutron scattering study. *Energy Fuel* 28, 6336–6344.
- Bahadur, J., Radlinski, A.P., Melnichenko, Y.B., Mastalerz, M., Schimmelmann, A., 2015. Small-angle and ultrasmall-angle neutron scattering (SANS/USANS) study of New Albany Shale: a treatise on microporosity. *Energy Fuel* 29, 567–576.
- Bajpayee, T., Pappas, D.M., Ellenberger, J.L., 2014. Roof instability: what reportable noninjury roof falls in underground coal mines can tell us. *Prof. Saf.* 59, 57.
- Bishop, A.W., Bjerrum, L., 1960. The relevance of the triaxial test to the solution of stability problems. In: ASCE Res. Conf. Shear Strength of Cohesive Soils. University of Colorado, pp. 437–501 1960.
- Bishop, A.W., Alpan, I., Blight, G., Donald, I., 1960. Factors controlling the strength of partly saturated cohesive soils. Conference Shear Strength Cohesive Soils. American Society of Civil Engineers: New York, 1960; 503–532.
- Brunauer, S., Deming, L.S., Deming, W.E., Teller, E., 1940. On a theory of the van der Waals adsorption of gases. *J. Am. Chem. Soc.* 62, 1723–1732.
- Bustin, R.M., Bustin, A.M., Cui, A., Ross, D., Pathi, V.M., et al., 2008. Impact of shale properties on pore structure and storage characteristics. In: SPE Shale Gas Production Conference, SPE, Fort Worth, Texas, USA (2008), pp. 28. <https://doi.org/10.2118/119892-MS>.
- Chalmers, G.R., Bustin, R.M., Power, I.M., 2012. Characterization of gas shale pore systems by porosimetry, pycnometry, surface area, and field emission scanning electron microscopy/transmission electron microscopy image analyses: examples from the Barnett, Woodford, Haynesville, Marcellus, and Doig units. *AAPG Bull.* 96, 1099–1119.
- Clarkson, C.R., Solano, N., Bustin, R., Bustin, A., Chalmers, G., He, L., Melnichenko, Y.B., Radlinski, A., Blach, T.P., 2013. Pore structure characterization of North American shale gas reservoirs using USANS/SANS, gas adsorption, and mercury intrusion. *Fuel* 103, 606–616.
- Conner, W.C., Lane, J.A., Hoffman, A., 1984. Measurement of the morphology of high surface area solids: hysteresis in mercury porosimetry. *J. Colloid Interface Sci.* 100, 185–193.
- Conner, W., Cavallos-Candau, J., Weist, E., Pajares, J., Mendioroz, S., Cortes, A., 1986. Characterization of pore structure: porosimetry and sorption. *Langmuir* 2, 151–154.
- Diamond, S., Kinter, E.B., 1958. Surface areas of clay minerals as derived from measurements of glycerol retention. *Clay Clay Miner.* 5, 334–347.
- Dieterich, M., Kutchko, B., Goodman, A., 2016. Characterization of Marcellus Shale and Huntersville Chert before and after exposure to hydraulic fracturing fluid via feature relocation using field-emission scanning electron microscopy. *Fuel* 182, 227–235.
- Esterhuizen, G., Bajpayee, T., others, 2012. Horizontal stress related failure in bedded mine roofs—insight from field observations and numerical models, in: 46th US Rock Mechanics/Geomechanics Symposium. American Rock Mechanics Association.
- Ferrari, A., Favero, V., Marschall, P., Laloui, L., 2014. Experimental analysis of the water retention behaviour of shales. *Int. J. Rock Mech. Min. Sci.* 72, 61–70.
- Giesche, H., 2006. Mercury porosimetry: a general (practical) overview. Part. Part. Syst. Charact. 23 (2006), 9–19.
- Gregg, S.J., Sing, K.S.W., 1982. Adsorption Surface Area and Porosity. 2nd edn. Academic Press, New York (303 pp.).
- Groen, J.C., Peffer, L.A., Pérez-Ramírez, J., 2003. Pore size determination in modified micro-and mesoporous materials. Pitfalls and limitations in gas adsorption data analysis. *Microporous Mesoporous Mater.* 60, 1–17.
- Hatch, J.R., Afolter, R.H., 2002. Resource Assessment of the Springfield, Herrin, Danville and Baker Coals in the Illinois Basin United States Geological Survey Professional Paper 1625-D (2002).
- Hatch, C.D., Wiese, J.S., Crane, C.C., Harris, K.J., Kloss, H.G., Baltrusaitis, J., 2012. Water adsorption on clay minerals as a function of relative humidity: application of BET and Freundlich adsorption models. *Langmuir* 28, 1790–1803.
- Hinde, A.L., 2004. PRINSAS—a Windows-based computer program for the processing and interpretation of small-angle scattering data tailored to the analysis of sedimentary rocks. *J. Appl. Crystallogr.* 37, 1020–1024.
- Iannacchione, A., Esterhuizen, G., Bajpayee, T., Swanson, P., Chapman, M., et al., 2005. Characteristics of mining-induced seismicity associated with roof falls and roof caving events Alaska Rocks 2005. In: The 40th US Symposium on Rock Mechanics (USRMS) (2005), pp. 1–10.
- Javadpour, F., Moravvej Farshi, M., Amrein, M., others, 2012. Atomic-force microscopy: a new tool for gas-shale characterization. *J. Can. Pet. Technol.* 51, 236–243.
- Kline, S.R., 2006. Reduction and analysis of SANS and USANS data using IGOR pro. *J. Appl. Crystallogr.* 39, 895–900.
- Kuila, U., Prasad, M., 2013. Specific surface area and pore-size distribution in clays and shales. *Geophys. Prospect.* 61, 341–362.
- Lowell, S., 1980. Continuous scan mercury porosimetry and the pore potential as a factor in porosimetry hysteresis. *Powder Technol.* 25, 37–43.
- Lowell, S., Shields, J.E., 1984. Theory of mercury porosimetry hysteresis. *Powder Technol.* 38, 121–124.
- Macht, F., Eusterhues, K., Pronk, G.J., Totsche, K.U., 2011. Specific surface area of clay minerals: Comparison between atomic force microscopy measurements and bulk-gas (N<sub>2</sub>) and-liquid (EGME) adsorption methods. *Appl. Clay Sci.* 53, 20–26.
- Mastalerz, M., He, L., Melnichenko, Y.B., Rupp, J.A., 2012. Porosity of coal and shale: Insights from gas adsorption and SANS/USANS techniques. *Energy Fuel* 26, 5109–5120.
- Melnichenko, Y.B., He, L., Sakurovs, R., Kholodenko, A.L., Blach, T., Mastalerz, M., Radlinski, A.P., Cheng, G., Mildner, D.F., 2012. Accessibility of pores in coal to methane and carbon dioxide. *Fuel* 91, 200–208.
- Mitchell, J., 1962. Components of pore water pressure and their engineering significance. In: Clays and Clay Minerals: Proceedings of the Ninth National Conference, pp. 162–184. <https://doi.org/10.1016/B978-1-4831-9842-2.50012-2>.
- Molinda, G.M., 2003. Geologic Hazards and Roof Stability in coal mines. Information Circular, IC9466. Dept. of Health and Human Services, Center for Disease Control and Prevention, NIOSH (2003).
- Murphy, M., 2016. Shale failure mechanics and intervention measures in underground coal mines: results from 50 years of ground control safety research. *Rock Mech. Rock Eng.* 49, 661–671.
- Newman, A., 1983. The specific surface of soils determined by water sorption. *Eur. J. Soil Sci.* 34, 23–32.
- Poulsen, B., Shen, B., Williams, D., Huddleston-Holmes, C., Erarslan, N., Qin, J., 2014. Strength reduction on saturation of coal and coal measures rocks with implications for coal pillar strength. *Int. J. Rock Mech. Min. Sci.* 71, 41–52.
- Powles, J., 1985. On the validity of the Kelvin equation. *J. Phys. A Math. Gen.* 18, 1551.
- Quirk, J., Aylmore, L., 1971. Domains and quasi-crystalline regions in clay systems. *Soil Sci. Soc. Am. J.* 35, 652–654.
- Radlinski, A.P., Radlinska, E.Z., 1999. The microstructure of pore space in coals of different rank. In: Mastalerz, M., Glikson, M., Golding, S.D. (Eds.), Coalbed Methane: Scientific, Environmental and Economic Evaluation. Springer, Dordrecht. [https://doi.org/10.1007/978-94-017-1062-6\\_20](https://doi.org/10.1007/978-94-017-1062-6_20).
- Radlinski, A., Boreham, C., Wignall, G., Lin, J.-S., 1996. Microstructural evolution of source rocks during hydrocarbon generation: a small-angle-scattering study. *Phys. Rev. B* 53, 14152.
- Radlinski, A., Radlinska, E., Agamalian, M., Wignall, G., Lindner, P., Randl, O., 1999. Fractal geometry of rocks. *Phys. Rev. Lett.* 82, 3078.
- Radlinski, A., Boreham, C., Lindner, P., Randl, O., Wignall, G., Hinde, A., Hope, J., 2000. Small angle neutron scattering signature of oil generation in artificially and naturally matured hydrocarbon source rocks. *Org. Geochem.* 31, 1–14.
- Radlinski, A., Mastalerz, M., Hinde, A., Hainbuchner, M., Rauch, H., Baron, M., Lin, J., Fan, L., Thiyagarajan, P., 2004. Application of SAXS and SANS in evaluation of porosity, pore size distribution and surface area of coal. *Int. J. Coal Geol.* 59, 245–271.
- Ruppert, L.F., Sakurovs, R., Blach, T.P., He, L., Melnichenko, Y.B., Mildner, D.F., Alcantar-Lopez, L., 2013. A USANS/SANS study of the accessibility of pores in the Barnett Shale to methane and water. *Energy Fuel* 27, 772–779.
- Schmitt, L., Forsans, T., Santarelli, F., 1994. Shale testing and capillary phenomena. *Int. J. Rock Mech. Min. Sci. Geomech. Abstr.* 31, 411–427. [https://doi.org/10.1016/0148-9062\(94\)90145-7](https://doi.org/10.1016/0148-9062(94)90145-7).
- Seemann, T., Bertier, P., Krooss, B.M., Stanjek, H., 2017. Water vapour sorption on mudrocks. *Geol. Soc. Lond., Spec. Publ.* 454, SP454–8.
- Sun, M., Yu, B., Hu, Q., Zhang, Y., Li, B., Yang, R., Melnichenko, Y.B., Cheng, G., 2017. Pore characteristics of Longmaxi shale gas reservoir in the Northwest of Guizhou, China: Investigations using small-angle neutron scattering (SANS), helium pycnometry, and gas sorption isotherm. *Int. J. Coal Geol.* 171, 61–68.
- Thommes, M., Morell, J., Cychosz, K.A., Fröba, M., 2013. Combining nitrogen, argon, and water adsorption for advanced characterization of ordered mesoporous carbons (CMKs) and periodic mesoporous organosilicas (PMOs). *Langmuir* 29, 14893–14902.
- Tong, S., Dong, Y., Zhang, Q., Elsworth, D., Liu, S., 2017. Quantitative analysis of nanopore structural characteristics of lower paleozoic shale, chongqing (Southwestern China): combining FIB-SEM and NMR cryoporometry. *Energy Fuel* 31, 13317–13328.
- Van Eckhout, E.M., 1976. The mechanisms of strength reduction due to moisture in coal mine shales. *Int. J. Rock Mech. Min. Sci. Geomech. Abstr.* 13, 61–67. [https://doi.org/10.1016/0148-9062\(76\)90705-1](https://doi.org/10.1016/0148-9062(76)90705-1).
- Van Eckhout, E.M., Peng, S.S., 1975. The effect of humidity on the compliances of coal mine shales. *Int. J. Rock Mech. Min. Sci. Geomech. Abstr.* 12, 335–340. [https://doi.org/10.1016/0148-9062\(75\)90166-7](https://doi.org/10.1016/0148-9062(75)90166-7).

- Wang, Y., Zhu, Y., Chen, S., Li, W., 2014. Characteristics of the nanoscale pore structure in Northwestern Hunan shale gas reservoirs using field emission scanning electron microscopy, high-pressure mercury intrusion, and gas adsorption. *Energy Fuel* 28, 945–955.
- Wang, Y., Zhu, Y., Liu, S., Zhang, R., 2016. Pore characterization and its impact on methane adsorption capacity for organic-rich marine shales. *Fuel* 181, 227–237.
- Wardlaw, N.C., McKellar, M., Yu, L., 1988. Pore and throat size distributions determined by mercury porosimetry and by direct observation. *Carbonates Evaporites* 3 (1).
- Washburn, E.W., 1921. Note on a method of determining the distribution of pore sizes in a porous material. *Proc. Natl. Acad. Sci.* 7, 115–116.
- Zhang, R., Liu, S., Bahadur, J., Elsworth, D., Melnichenko, Y., He, L., Wang, Y., 2015. Estimation and modeling of coal pore accessibility using small angle neutron scattering. *Fuel* 161, 323–332.
- Zhang, Q., Dong, Y., Liu, S., Elsworth, D., Zhao, Y., 2017a. Shale pore characterization using NMR cryoporometry with octamethylcyclotetrasiloxane as the probe liquid. *Energy Fuel* 31, 6951–6959.
- Zhang, R., Liu, S., Wang, Y., 2017b. Fractal evolution under in situ pressure and sorption conditions for coal and shale. *Sci. Rep.* 7, 8971.
- Zhao, Y., Liu, S., Elsworth, D., Jiang, Y., Zhu, J., 2014. Pore structure characterization of coal by synchrotron small-angle X-ray scattering and transmission electron microscopy. *Energy Fuel* 28, 3704–3711.